



Investigation of Dust Grains by Optical Tweezers for Space Applications

A. Magazzù¹, D. Bronte Ciriza^{1,2}, A. Musolino^{3,4}, A. Saidi², P. Polimeno^{1,2}, M. G. Donato¹, A. Foti¹, P. G. Gucciardi¹, M. A. Iati¹, R. Saija², N. Perchiazzi³, A. Rotundi⁵, L. Folco^{3,6}, and O. M. Maragò¹

¹CNR-IPCF, Istituto per i Processi Chimico-Fisici, Messina, Italy; magazzu@ipcf.cnr.it

²Dipartimento di Scienze Matematiche e Informatiche, Scienze Fisiche e Scienze della Terra, Università di Messina, Italy

³Dipartimento di Scienze della Terra, Università di Pisa, Pisa, Italy

⁴INAF-IAPS, Istituto Nazionale di Astrofisica, Istituto di Astrofisica e Planetologia Spaziali, Rome, Italy

⁵Dipartimento di Scienze e Tecnologie, Università degli studi di Napoli Parthenope, Italy

⁶CISUP, Center for Instrument Sharing of the University of Pisa, Università di Pisa, Italy

Received 2022 June 24; revised 2022 September 8; accepted 2022 October 9; published 2022 December 28

Abstract

Cosmic dust plays a dominant role in the universe, especially in the formation of stars and planetary systems. Furthermore, the surface of cosmic dust grains is the benchwork where molecular hydrogen and simple organic compounds are formed. We manipulate individual dust particles in a water solution by contactless and noninvasive techniques such as standard optical and Raman tweezers, to characterize their response to mechanical effects of light (optical forces and torques) and to determine their mineral compositions. Moreover, we show accurate optical force calculations in the T-matrix formalism highlighting the key role of composition and complex morphology in the optical trapping of cosmic dust particles. This opens perspectives for future applications of optical tweezers in curation facilities for sample-return missions or in extraterrestrial environments.

Key words: Interplanetary dust – Meteoroid dust clouds – Solid matter physics

1. Introduction

In the frame of astrophysical science and its related technology (space missions, optical and radio telescopes), cosmic dust has attracted the interest of scientists due to its role in the cycling processes active in the universe. Cosmic dust is a comprehensive term indicating small solid particles with sizes ranging from a few nanometers to tenths of a millimeter. They are floating around in the interstellar medium or in the interplanetary space in the solar system. Interstellar dust is mainly generated by the lifecycles of many generations of stars: it is released by radiation pressure and solar wind or ejected during the end-time explosion of stars or during the blowing off of their outer layers (Woosley & Weaver 1995; Woosley et al. 2002; Calura et al. 2008). Interplanetary dust consists of small solid particles generated by collisions between solid bodies (e.g., asteroids, planets, and their satellites) or evaporation of icy bodies (e.g., comets) (Rietmeijer 1998). If interstellar dust is almost exclusively analyzed through remote observations (Draine 2003; Lodders & Amari 2005), on the other hand, interplanetary dust is available through sample-return space missions from interplanetary medium, planets, and minor bodies (Brownlee et al. 2003; Frank et al. 2014; Westphal et al. 2014), from the Earth's stratosphere (Testa et al. 1990; Taylor et al. 1996; Della Corte et al. 2012; Lauretta et al. 2017) and at the Earth's surface in the form of micrometeorites (e.g., Genge et al. 2008; Folco & Cordier 2015; Taylor et al. 2016). Samples are analyzed at terrestrial facilities by state-of-the-art analytical techniques—since the size of some instruments is still too large to fly to the space (Rietmeijer 2001; Rauf et al. 2010; Della Corte et al. 2014).

Physicochemical properties of cosmic dust can be studied by different techniques, such as X-rays diffraction (Mackinnon & Rietmeijer 1987), scanning electron microscopy (SEM), transmission electron microscopy (Lewis et al. 1987), IR, Raman (Rotundi et al. 2008; Davidson et al. 2012), and mass spectroscopy (Floss et al. 2006). However, these techniques may induce shielding effects by the substrates or by other particles. In this work, to overcome these unwanted effects, we develop and test our setups of optical and Raman tweezers, which are contactless and nondestructive techniques useful for the manipulation and investigation of individual grains of cosmic dust (Alali et al. 2020). Optical tweezers (OT) are tools based on focused laser beams, which allow the trapping and manipulation of microparticles and nanoparticles without a physical contact (Jones et al. 2015). This contactless and nondestructive technique in its simplest configuration is based on a single laser beam focused down to the diffraction limit by a high numerical aperture (NA) objective (Ashkin & Dziedzic 1971; Ashkin et al. 1986). Optical forces are strongly dependent on particle size, shape, and composition (see also Appendix A). However, OT enable trapping and characterization of particles in a wide size range, from single atoms to cells (Jones et al. 2015; Polimeno et al. 2018). Furthermore, Raman tweezers, i.e., OT coupled to a Raman spectrometer, are able to spectroscopically characterize optically trapped samples allowing accurate information on their composition (Thurn & Kiefer 1984; Lankers et al. 1994; Pan et al. 2012; Gong et al. 2018; Gillibert et al. 2019).

Here, we characterize the dust particle response to optical forces and torques, providing accurate information on the particle dynamics in the optical trap. Furthermore, we identify dust particle mineralogical compositions by Raman tweezers. We compare our findings with optical force calculations based on the T-matrix formalism showing how the composition and the complex shape of dust particles play a key role in their light-driven dynamics.



Original content from this work may be used under the terms of the [Creative Commons Attribution 4.0 licence](https://creativecommons.org/licenses/by/4.0/). Any further distribution of this work must maintain attribution to the author(s) and the title of the work, journal citation and DOI.

2. Materials and Methods

The samples trapped and characterized with our Raman tweezers have known textures and mineralogic compositions documented in this work and in previous studies. The aim is to reproduce the well-known composition of the trapped particles to validate the application of optical manipulation techniques to cosmic dust.

The samples used have terrestrial and extraterrestrial origins. They are (1) a quartzarenite (M26) from Kamil Crater in Egypt (Fazio et al. 2014), (2) a hawaiiite (HE-1) from Etna volcano in Italy, (3) the CV3-OxA carbonaceous chondrite (A-1) from Allende meteorite, and (4) a lunar meteorite (DEW 12007) (polymict regolith breccia) found in Antarctica (Collareta et al. 2016). Previously, mineral grains used to calibrate the dust analyzer Giada on board Rosetta space mission (Colangeli et al. 2007) were used as the simplest possible starting material (monomineralic, uniform size range). In this work, we have chosen more complex nonuniform samples: the terrestrial rocks M-26 and HE-1, considered inasmuch analogs of planetary materials (monomineralic and polymineralic); and the extraterrestrial rocks as representative of primitive (A-1) and differentiated (DEW 12007) bodies of the solar system.

Once powdered, the samples are analyzed using micro-analytical SEM for a textural characterization (shape, grain-size). Their main mineralogy is determined using X-ray powder diffraction (Appendix D). The characterization was conducted at the Dipartimento di Scienze della Terra and at the Center for Instrument Sharing of the University of Pisa (CISUP).

All the analyzed samples were provided as dried powder, whose grains showed a nonhomogeneous size and shape distribution, as shown in Figures 1(a), (d). The first step of the sample preparation was the dispersion of the powder in distilled water by ultrasound sonication with an appropriate concentration suitable for optical trapping (e.g., few particles per microliter). The water–dust solution was then placed in a glass cavity slide and sealed by a coverglass, as shown in Figures 1(b), (c). The sealed cavity glass slide was then placed on the sample holder of our OT for the investigation (Figure 1(c)). For the investigation of individual grain dust particles dispersed in water, we used two different customized setups: (i) standard OT, where an optical trap was generated by highly focusing a laser beam through an objective, where the trajectory of the trapped particle was acquired by a quadrant photodiode (QPD) and analyzed by a computer to calculate optical forces and rotations arising from the interaction of the particle with light (Figure 1(e)); (ii) Raman tweezers, where the back-scattered light from the particle was collected through the same focusing objective and reflected to a Raman spectrometer for phase identification (Figure 1(f)). See Appendix B for more details.

3. Results

3.1. Optical Forces and Torques on Dust Particles

The output signals from the QPD, proportional to the particle displacement of the trapped particle from its equilibrium position, are analyzed by MATLAB routines to calculate the trap stiffness and to detect any rotation of the particle in the perpendicular plane $x - y$. In particular, we use the autocorrelation functions and power spectral density (PSD) calibration methods (Jones et al. 2015; Gieseler et al. 2021) to obtain the relaxation frequencies of the trapped particles as fitted parameters and hence to calculate the trap stiffness (Figures 6(b), 2(a)), see

Appendix B for more details. We observe that the stiffness of terrestrial and extraterrestrial samples, optically trapped by linear polarized (LP) light, increases with the laser power, as shown in Figure 2(a) for a single trapped grain of the lunar meteorite DEW 12007. Here it is possible to notice that the stiffnesses κ_x , κ_y , and κ_z increase almost linearly with the laser power, and the difference between the stiffnesses along the x - and y -directions can be due to a possible asymmetry of the trapped grain with respect to the propagation axis z . Usually the values of the stiffness κ_z are lower than the values of κ_x and κ_y due to the longer extension of the Gaussian beam along the z -axis (Jones et al. 2015). Due to the linearity of the stiffness with power, it is possible to obtain the stiffness efficiency $q_i = k_i/Pw$ (with $i = x, y, z$) as a fitting parameter from the values of κ_i reported in Figure 2(a), where Pw is the value of the laser power measured at the objective output by a power meter. In particular, by a linear fit, we obtain that $q_x = 1.38 \text{ pN}\mu\text{m}^{-1}\text{mW}^{-1}$, $q_y = 1.10 \text{ pN}\mu\text{m}^{-1}\text{mW}^{-1}$, and $q_z = 0.54 \text{ pN}\mu\text{m}^{-1}\text{mW}^{-1}$ respectively. Radiation pressure on complex shaped or absorbing particles can also have a destabilizing effect by pushing the trapped particles in regions of lower intensity along the z -axis. For example, grains from Allende meteorite are difficult to trap in 3D and were often investigated while trapped in 2D against the cell wall.

In order to compare our experimental results with theoretical expectations, we calculate optical forces through the Maxwell stress tensor exploiting the multipole expansion and T-matrix formalism (Borghese et al. 2007a; Polimeno et al. 2018, 2021). We consider particle models emulating the dust grains of the lunar meteorite DEW 12007. Although all the trapped dust grains showed irregular shapes, for simplicity, we modeled our particles as microspheres having an average diameter $d = 1 \mu\text{m}$ with a refractive index given by the Bruggeman mixing rule for the constituent minerals of DEW 12007, as shown in the inset of Figure 3(a) (Bohren & Huffman 2008; Polimeno et al. 2021).

In our calculations, we consider a single Gaussian laser beam having a wavelength $\lambda = 830 \text{ nm}$ and a power $Pw = 50 \text{ mW}$, focused by a high-NA objective (NA=1.3), mimicking the experimental conditions used during the investigation of the lunar dust grains. In Figure 3(a), we show the theoretical transversal and longitudinal trap efficiencies defined respectively as follows: $Q_{xy}^{\text{th}} = (F_x^{\text{opt}} + F_y^{\text{opt}})/2Pw$, and $Q_z^{\text{th}} = F_z^{\text{opt}}/Pw$. Thereafter, we refined our particle model to take into account the anisotropy and heterogeneity of the real dust grains. We still considered an homogeneous sphere, with a refractive index obtained according to the Bruggeman mixing rule, but now we add 4 spherical inclusions; see Figure 3(b), inset. These inclusions are made of the secondary constituents of the lunar meteorite; in particular we consider 2 inclusions made of olivine having 10% each of the total volume of the modeled grain, and 2 inclusions of ilmenite with 2% each of the total volume. Similarly to the previous model, we calculate the optical forces and the theoretical longitudinal trap efficiency Q_z^{th} , as shown in Figure 3(b). Here it is possible to notice how the trap efficiency is affected by the internal structure of a dust grain, presenting several equilibrium points with $Q_z^{\text{th}} = 0$, and only two stable equilibrium points at $z = -0.38 \mu\text{m}$, and $z = 0.75 \mu\text{m}$; conversely, the homogeneous model was showing an only stable equilibrium point at $z = 0 \mu\text{m}$; see Figures 3(a), (b).

Aiming at validating our theoretical model, we compare the theoretical $q_{xy,z}^{\text{th}}$ and experimental $q_{xy,z}^{\text{ex}}$ stiffness efficiencies on the transverse $x - y$ plane and in the longitudinal direction z . In particular, in the former case, the mean transverse efficiency

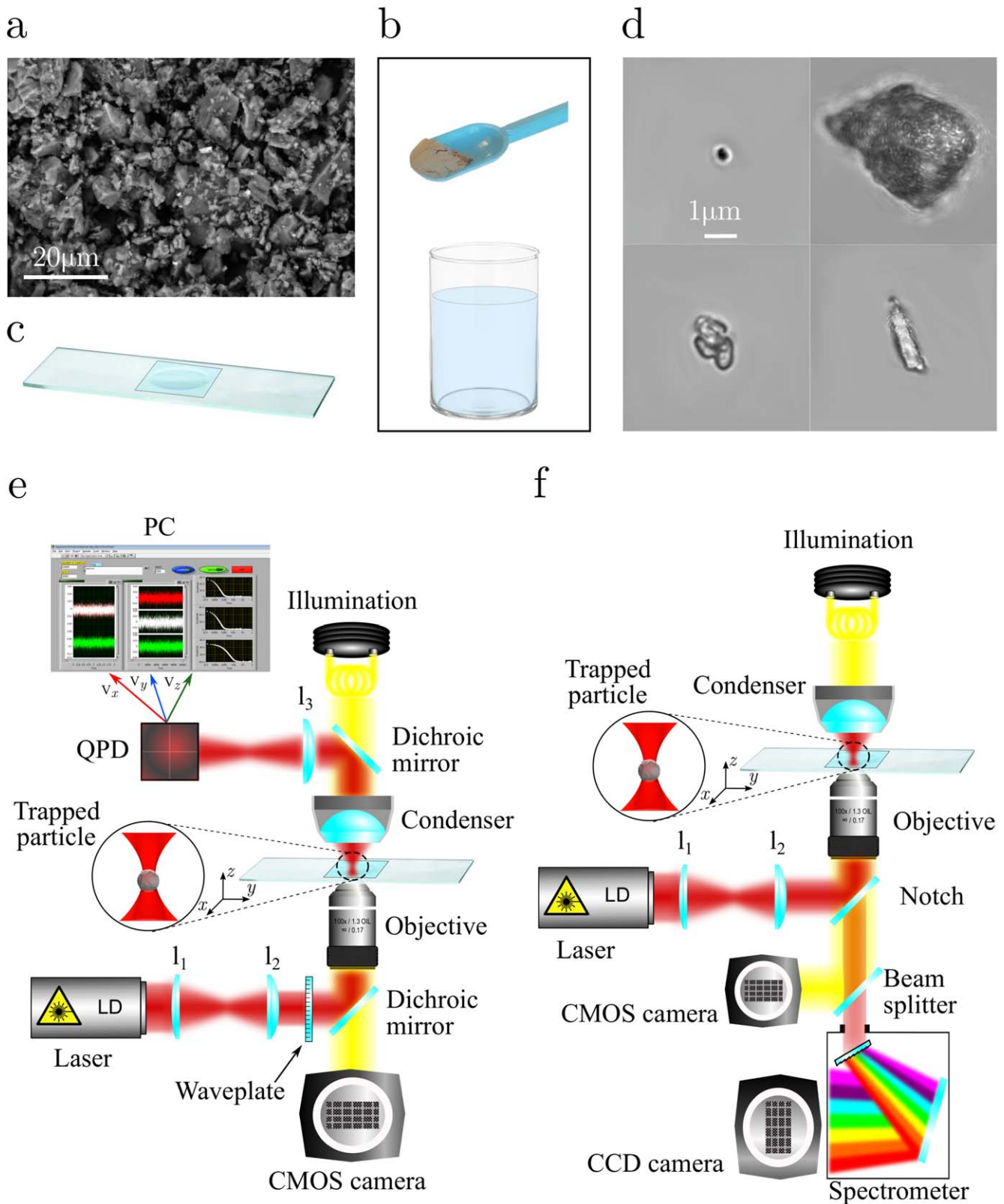


Figure 1. Samples preparation and sketch of the experimental setups. (a) SEM image of DEW 12007 lunar meteorite powdered sample, showing the polycrystalline nature of each individual grain. (b) Dust samples are dispersed in distilled water by ultrasound sonication, and (c) this solution is placed within a cavity glass slide and sealed by a coverglass. (d) Screenshots of four different 3D optically trapped grains of cosmic dust in water solution having different size and morphology. (e) Standard optical tweezers setup. (f) Raman tweezers setup.

$q_{xy} = (q_x + q_y)/2$ is considered. Moreover, in the case of the theoretical stiffness efficiencies, P_w is the value of the power set for the simulation.

In Figure 3(c), it is possible to notice a relative good agreement between the theoretical and experimental values of the stiffness efficiencies q^{th} and q^{ex} , validating the theoretical

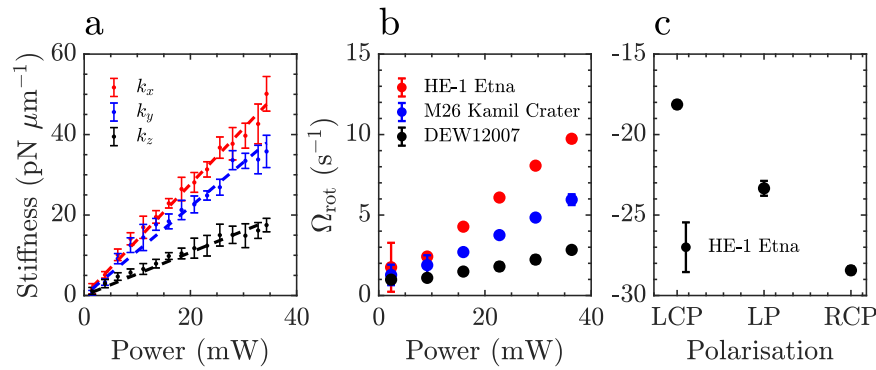


Figure 2. Effects of the laser light on trapped particles. (a) Trap stiffnesses κ_x , κ_y , and κ_z as a function of the laser power measured at the objective for a single trapped grain of the lunar meteorite DEW 12007. (b) Rotational frequencies Ω_{rot} of different samples as a function of the laser power measured at the objective. (c) Rotational frequencies, Ω_{rot} , of an optically trapped single dust grain of HE-1 for different polarized light: left circular polarized (LCP), linear polarized (LP), and right circular polarized (RCP) light. Negative–positive frequency values correspond to a rotation counterclockwise–clockwise with respect to the z -axis, respectively.

model used for the calculation of optical forces acting on cosmic dust. The small discrepancies are due to the spherical shape used in our model, which is a simplification of the complex particle shape, mass distribution, and mineral composition. In fact, a linearly polarized laser light does not produce any radiation torque on a spherical and homogeneous particle because of symmetry (Marston & Crichton 1984). However, for anisotropic and asymmetric particles, two additional mechanical effects of light occur: (i) a transverse component of radiation pressure, which is responsible for the *optical lift effect*, i.e., a transverse displacement of the particle with respect to the incident light propagation direction (Swartzlander et al. 2011); (ii) a radiation pressure torque inducing particle rotations and known as the *windmill effect* (Jones et al. 2015).

Rotations of a trapped particle induce a correlation among its x , y trajectories. In these circumstances, we can use OT also for photonic torque microscopy to quantify these rotations (Irrera et al. 2016; Schmidt et al. 2018). In particular, particle rotations in the x – y plane can be highlighted by calculating the differential cross correlations $\text{DCCF}_{xy}(\tau) = \langle x(t)y(t+\tau) \rangle - \langle y(t)x(t+\tau) \rangle$ of the acquired signal from the QPD, Figure 6(a) in Appendix B, for different lag times τ . The rotational frequency Ω_{rot} can be obtained as a fitting parameter of the DCCF_{xy} by a sinusoidal model (Jones et al. 2009; Pesce et al. 2009).

In Figure 2(b), we show the rotational frequency Ω_{rot} of three different trapped samples, where Ω_{rot} increases as the laser power increases. It is noteworthy that the polarization used to trap the samples listed in Figure 2(b) is linear, it does not carry any spin-angular momentum, so the observed rotations are only due to the radiation torque exerted by the light on the particles because of their asymmetric shape.

In the case of circular polarized light, depending on the absorption properties of the particle, a laser beam can induce a spin-angular torque in addition to the radiation one (Marston & Crichton 1984; Jones et al. 2015). When a laser beam is circularly polarized, each of its photons carries a spin-angular momentum $+\hbar$ for left circularly polarized (LCP) light, $-\hbar$ for right circularly polarized (RCP) light. Therefore, the total torque acting on a nonspherical particle is given by different contributions that include a radiation torque related to the shape and the transferred spin-angular momentum. The spin-angular momentum is added to the windmill effect in the case of LCP and subtracted in the case of RCP (Jones et al. 2015).

In Figure 2(c), we report the rotational frequency Ω_{rot} of an optically trapped grain of the terrestrial samples HE-1 from Etna volcano for different light polarization. Here, Ω_{rot} decreases from -18 s^{-1} for LCP to -28 s^{-1} for RCP with a central value of -23 s^{-1} for LP indicating that the trapped particle is absorbing circular polarized light with a spin-angular momentum $+\hbar$ for LCP light and $-\hbar$ for RCP light. Thus, negative frequency values mean a rotation counterclockwise with respect to the z -axis, while positive frequency values mean a rotation clockwise with respect to the z -axis. The rotational frequency Ω_{rot} reported in Figure 2(c) is the result of rotations induced by the total torque acting on the sample. The radiation pressure torque, which does not depend on light polarization, produces a particle rotation frequency of -23 s^{-1} , while the spin-angular momentum torque sums or subtracts depending on the helicity of light. In the case of LCP light, the contribution of the spin-angular momentum torque is positive and summed to the radiation torque increasing the rotational frequency of the particle to -18 s^{-1} , while in the case of RCP light the contribution is negative, decreasing the rotational frequency of the particle to -28 s^{-1} . This demonstrates that the total opto–mechanical interaction of particles with light, depends both on the particle shape and on the helicity of the laser beam.

3.2. Spectroscopic Analysis and Mineralogy of Individual Grains

We characterize the mineralogical compositions of terrestrial and extraterrestrial dust grains with different shapes and sizes by Raman tweezers; see Figure 1(d). All the investigated samples are trapped in 3D or in 2D, whenever the radiation pressure is stronger than the axial gradient force. In the latter case, a stable 3D optical trapping is not achievable because the radiation pressure pushes the particle away along the z -direction, along which the laser beam propagates. To overcome this issue, we push the particle against the wall of the glass slide, thereby physically confining the particle along the z -direction, while the particle is still confined along the x - and y -direction by the optical gradient forces, defining the optical potential. For each sample, a reference background spectrum, without any trapped particle, is also acquired and used to remove the spurious signal from the glass slide and the media (water, immersion oil). Thereafter, by a fitting routine, the peaks of each spectrum are identified and compared with reference spectra for the identification of the constituent phases in the

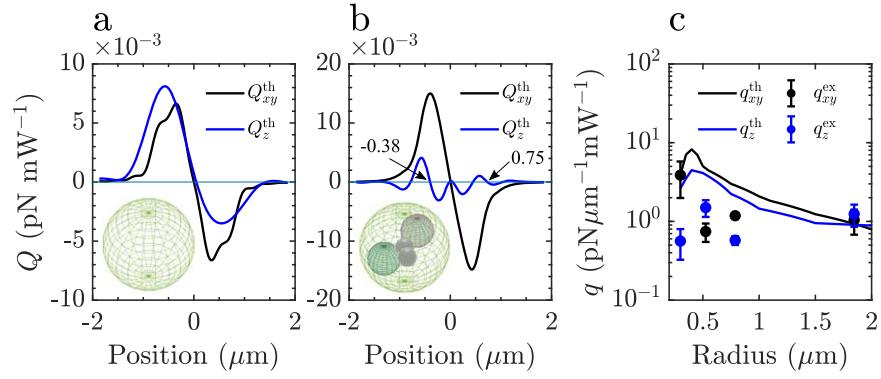


Figure 3. Theoretical trap efficiencies. (a) Black line represents the theoretical trap efficiency along the transversal direction $x-y$ with $z = 0$. Dark blue line represents the theoretical trap efficiency Q_z^{th} along the longitudinal direction z with $x = y = 0$. Shown in the inset, the theoretical particle, modeled as a microsphere with homogeneous refractive index according to the Bruggeman mixing rule. Light blue line is a reference line at $y = 0$. (b) Black and blue lines represent the theoretical trap efficiencies Q_{xy}^{th} and Q_z^{th} , respectively, for a particle model shown in the inset. Here the particle is modeled again as a microsphere with homogeneous refractive index according to the Bruggeman mixing rule but has 4 inclusions made of the secondary constituents of the lunar meteorite, 2 inclusions made of olivine having 10% each of the total volume, and 2 inclusions of ilmenite with 2% each of the volume. Q_z^{th} presents only two stable equilibrium points at $z = -0.38 \mu\text{m}$ and $z = 0.75 \mu\text{m}$, but, according to our forces calculations, only at $z = 0.75 \mu\text{m}$ trapping along the x - and y -directions is possible. (c) Theoretical (lines) and experimental (dots) stiffness efficiencies q_{xy} (black) and q_z (blue) within the transversal plane $x-y$ and along the longitudinal direction z respectively.

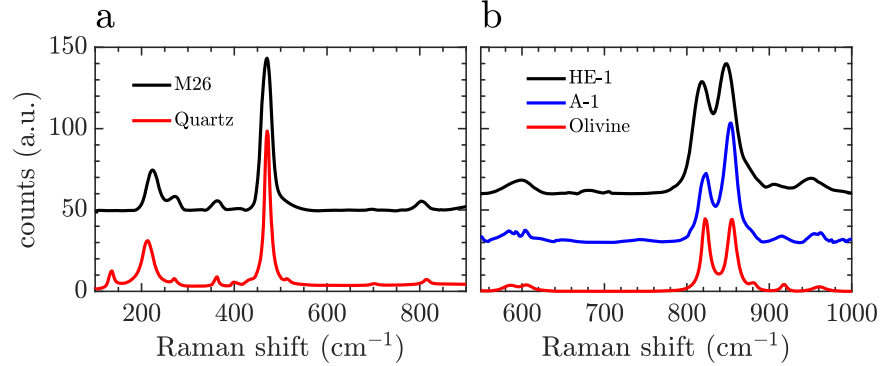


Figure 4. Raman spectra of optically trapped single dust particle from sample: (a) M26 from Kamil crater (black line); red line represents the Raman spectrum of quartz used as reference (RRUFF R150074). (b) HE-1 from Etna (black line), and A-1 from Allende meteorite (blue line). Red line represents the Raman spectrum of olivine used as standard reference (RRUFF X050088). All spectra are offset for clarity.

trapped samples. We first analyze the standard samples M26, HE-1, and A-1 in order to match their mineral composition reported in literature (Cristofolini et al. 1987; Orlando et al. 2008; Brunetto et al. 2014; Fazio et al. 2014).

In Figure 4(a), we report a Raman spectrum (black line) collected by a single optically trapped grain of sample M26. According to the literature, it contains mainly quartz whose reference spectrum is represented by the red line (Fazio et al. 2014). Similarly, in Figure 4(b), we report the Raman spectra, of a single grain of the sample HE-1 from Etna volcano (black line) and of A-1 from Allende meteorite (blue line). According to the literature, both meteorites contain olivine, whose reference spectrum is represented by the red line (Cristofolini et al. 1987). For all the experimental spectra of our samples shown in Figures 4(a), (b), there is a good agreement with the reference spectra of their mineral composition found in literature.

After testing our Raman tweezers on terrestrial and extra-terrestrial standard grains, we investigate cosmic dust from the lunar meteorite DEW 12007. In particular, we trap about 70 different particles in 2D and 3D, following an appropriate protocol to avoid trapping the same grains twice. In Figures 5(a)–(d), we report with black lines the Raman spectra of four different trapped grains of DEW 12007, and with

colored lines the reference Raman spectra of some of their constituents according to the literature (Collareta et al. 2016). In particular, in Figures 5(a)–(d), we can observe that the trapped grains contain the following minerals: plagioclase (labradorite); pyroxene (augite and pigeonite); olivine (forsterite and fayalite); ilmenite.

Figures 4(a), (b), and 5(a)–(d) show that each single trapped grain contains only a single mineral component, among the several ones reported in literature, matching its own reference spectrum. We identified both monomineralic and polymineralic grains (Figure 5(e)), as expected for a rock in which the grain-size is highly variable.

The occurrence of the mineral constituents of the lunar meteorite DEW 12007 over 70 dust grains is reported in Figure 5(f), where it is possible to notice that plagioclase is the most recurring mineral constituent, with an occurrence of 50.5%; then we found that pyroxene is the second most abundant mineral with an occurrence of 27.8%, and finally olivine and ilmenite with an abundance of 11.3% and 10.4% respectively. The rank of the mineral abundances of the constituents of DEW 12007 matches the data from the literature (Collareta et al. 2016). It is noteworthy that during the grinding process it could happen that cosmic dust was not

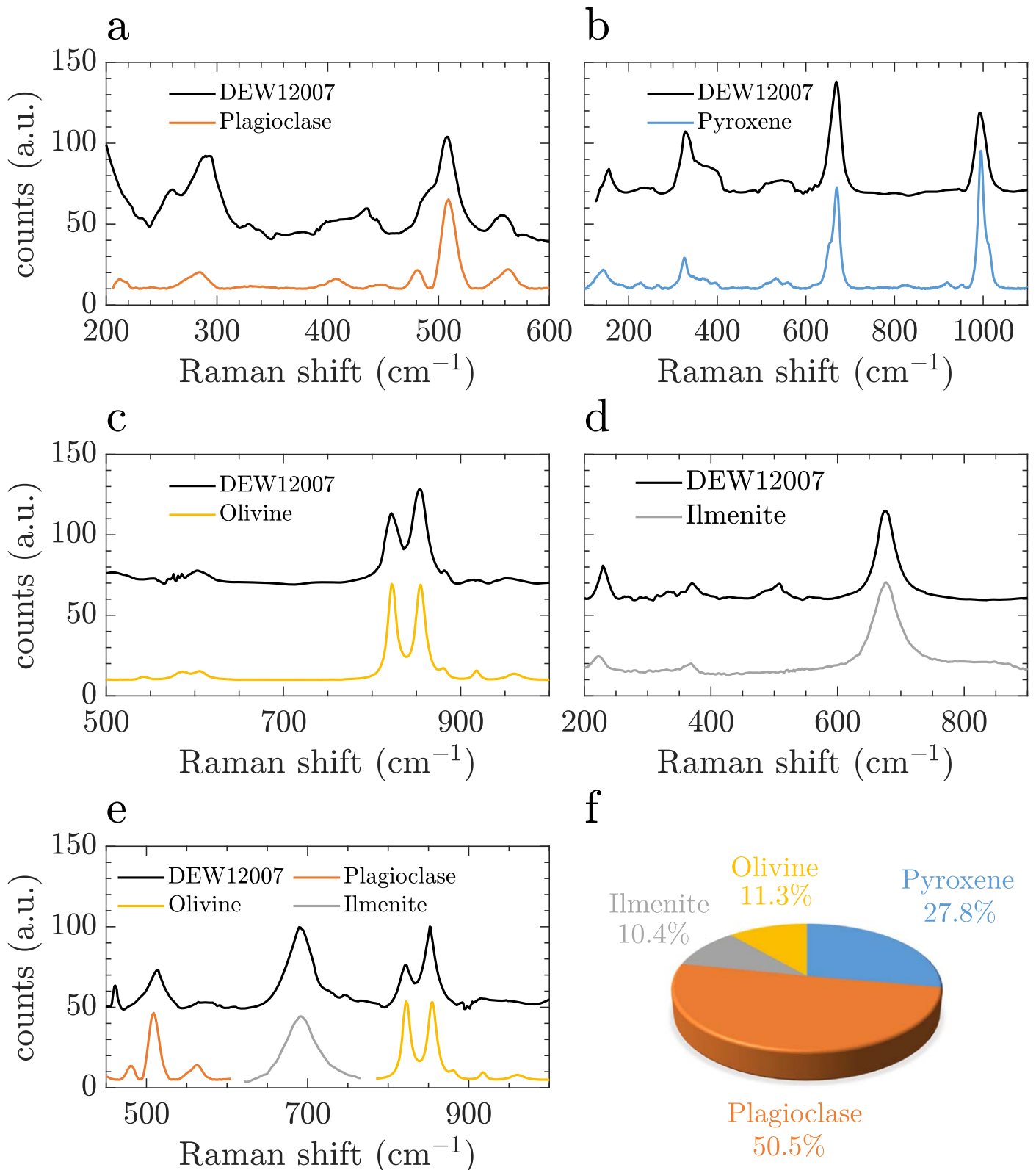


Figure 5. Raman spectra and mineralogical composition of optically trapped dust particles of the lunar meteorite DEW 12007. Black lines represent the Raman spectra of the trapped samples, while colored lines represent the reference Raman spectra from the RRUFF database of: (a) plagioclase (RRUFF X050108), (b) pyroxene (RRUFF R200002), (c) olivine (RRUFF X050088), and (d) ilmenite (RRUFF R060149), used for the mineral identification of the trapped single grains. All spectra are offset for clarity. (e) Raman spectra of a single grain of DEW 12007 (black line) containing several mineral components (colored lines). (f) Mineral occurrence of the mineral constituents over 70 trapped grains of the lunar meteorite DEW 12007.

homogeneously ground, producing grains with more than one or without any clear mineral component.

4. Conclusions

We used OT to trap individual micron-sized dust particles of astrophysical interest to characterize their opto-mechanical response. We calculated their trap stiffness and their rotational frequencies as a function of the trapping laser power, showing how these quantities increase almost linearly with the laser power. We also calculated the theoretical values of the optical forces acting on cosmic dust by T-matrix formalism, finding a good agreement between the experimental and theoretical values, validating our theoretical models. Moreover, we investigated the effect of light polarization on cosmic dust, measuring the particle rotational frequency for the different helicity of light, showing how the total opto-mechanical interaction depends on both the particle shape and the polarization of the laser beam. Furthermore, we used Raman tweezers to investigate the mineral composition of the dust particles. The agreement of our results with the literature validates optical trapping for the analysis of cosmic dust, opening new perspectives in the investigation of extraterrestrial particles on our planet. Optical trapping techniques, thanks to their contactless and noninvasive unique combination of capabilities, can be used to maximize the scientific return from the analyses of cosmic dust samples collected by the current and future sample-return missions (e.g., OSIRIS-Rex, Mars 2020; Chang’e 5), particularly during the preliminary investigation procedures in receiving-curation facilities (Smith et al. 2021). The high-resolution, contactless, and noninvasive analyses of planetary dust are actually expected to provide unprecedented information on the astrophysical origin and geologic evolution of their parent bodies. Furthermore, they are also expected to be instrumental for biohazard assessment for constrained sample-return missions—like those targeting Mars or the icy bodies in the outer solar system, and the detection of past or extant extraterrestrial life. Finally, the successful trapping of particles in a water medium is the first step toward the realization of trapping in air-vacuum, a totally noninvasive micromanipulation fundamental for extraterrestrial materials. For these reasons, OT are key tools in controlled laboratory experiments, aiming for space applications to trap and characterize dust particles directly in space or on extraterrestrial bodies during exploratory missions.

We acknowledge financial contribution from the agreement between Agenzia Spaziale Italiana (ASI) and Istituto Nazionale di Astrofisica (INAF) n.2018-16-HH.0, project “SPACE Tweezers” and from the MSCA innovative training network (ITN) project “ActiveMatter” sponsored by the European Commission (Horizon 2020, Project Number 812780). A. Musolino acknowledges support by ASI-INAF, “Rosetta GIADA,” I/024/12/0. The lunar regolith breccia was collected during the 2017 Antarctic Campaign of the Programma Nazionale delle Ricerche in Antartide (PNRA) within the “Meteoriti Antartiche” project (ID: PNRA16_00029), and the sample used in this study was provided by the Museo Nazionale dell’Antartide di Siena. SEM imaging was carried out at the ESEM-FEG facility of the Centro per la Integrazione della Strumentazione—Università di Pisa (CISUP). A. Magazzù, D. Bronte Ciriza, and A. Musolino contributed equally to this work.

Appendix A Optical Forces

Forces arising in optical trapping are a consequence of the conservation of the electromagnetic momentum in the light-matter interaction (Jones et al. 2015). However, some simplifications and approximations have been made for an easier understanding of optical forces. These approximate approaches are often a valuable source of physical insight and have a great pedagogical value (Jones et al. 2015; Magazzù et al. 2015; Polimeno et al. 2018). In the geometrical optics approximation, valid for particle size larger than the wavelength of the trapping beam, optical forces can be divided in a gradient and a scattering component. The gradient force component is perpendicular to the propagation of the laser beam, it is proportional to the intensity gradient of the laser spot, and it is responsible for trapping, while the scattering force component, having the same direction of the propagating laser beam, is proportional to the light intensity and tends to push particles away from the laser focus due to the radiation pressure (Jones et al. 2015). In this approximation, the incoming optical field can be considered as a collection of light rays, each of them carrying a portion of the total optical power and linear momentum. When a ray impinges on a particle, it is partly transmitted and partly reflected by the particle surface, and the exchange of linear momentum between the ray and the particle generates an optical force $\vec{F} = \frac{\Delta\vec{P}}{\Delta t}$, where $\Delta\vec{P} = \vec{P}_{\text{inc}} - \vec{P}_{\text{ref}}$ is the exchanged momentum calculated as the difference between the incident and reflected momentum \vec{P}_{inc} and \vec{P}_{ref} respectively during a time interval Δt . The optical force exerted by a laser beam on a particle is the sum of the forces generated by each constituting ray, and for specific experimental conditions and parameters (e.g., when the refractive index of a particle is higher than the one of its surrounding medium, proper size of the particle and laser power, etc.), these forces can confine a particle within an equilibrium region close to the focal spot, where the force acting on the particle is zero (Jones et al. 2015; Magazzù et al. 2015; Polimeno et al. 2018). When a trapped particle is displaced from the center of the trap to a nonequilibrium point, a net optical force acts like a restoring spring, bringing the particle back toward the center of the trap. For a small displacement of the particle from its equilibrium position, the restoring force is, to a first approximation, proportional to the displacement acting like a Hookean spring with a fixed stiffness (Jones et al. 2015; Gieseler et al. 2021), i.e.

$$F_x \approx -\kappa_x(x - x_{\text{eq}}) \quad (\text{A1})$$

where, considering for simplicity only a single component of the force, x is the particle position, x_{eq} is the equilibrium position, and κ_x is the trap stiffness. The trap stiffness can be obtained by several calibration methods (Jones et al. 2015; Gieseler et al. 2021), and by its value we can quantify an external force $F_{\text{ext},x}$ acting on a trapped particle by measuring the particle displacement $\Delta x_{\text{eq}} = (x - x_{\text{eq}})$ from its equilibrium position, i.e., $F_{\text{ext},x} = \kappa_x \Delta x_{\text{eq}}$.

Appendix B Experimental Setups

The light source of the standard OT used for the investigation of cosmic dust is a laser diode (LD) generating a linear polarized laser beam with a wavelength of 830 nm. The laser beam is expanded by a two-lense (l_1 , l_2) telescope system and reflected by a dichroic mirror toward the back aperture of a high NA oil

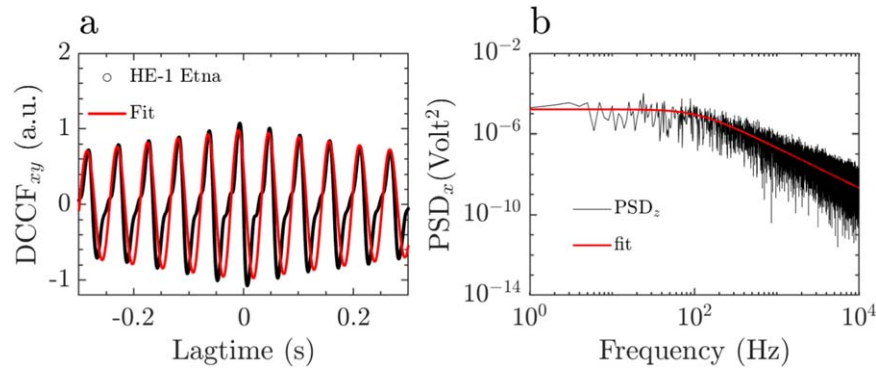


Figure 6. Rotational and relaxation frequencies. (a) Differential cross correlation function $DCCF_{xy}(\tau)$ of the sample HE-1 from Etna; black circles represent experimental data, while red line represents a sinusoidal fitting function. Discrepancy between the experimental data and the fit is due to the presence of a second rotational or vibrational motion of the trapped particle due to its nonspherical geometry and anisotropy (Jones et al. 2009). (b) Black line represents the power spectrum density (PSD) of the trajectory along z -direction for a trapped dust grain of the lunar meteorite DEW 12007, while the red line represents a Lorentzian fit of the calculated PSD, where the relaxation frequency of the trapped grain is obtained as fitted parameter.

immersion objective, which was also used to imagine the sample on a CMOS camera; see Figure 1(e). Thanks to the telescope system, the beam overfills the back aperture of the objective giving rise to a highly focused laser beam. The overfilling creates the maximal optical field gradient in the focal spot for a more efficient optical trapping. A sample holder is equipped with a 3D translation piezo-stage to move the focal spot within the cavity glass slide containing the sample solution. The dichroic mirror used to reflect the laser beam to the objective acts like a short pass filter, it reflects the laser light toward the objective and transmits the visible light to a CMOS camera, preventing the saturation of the detector and allowing a clear view of the sample on a monitor. The polarization of the trapping beam can be tuned by a wave plate to investigate the optical response of cosmic dust for different light polarizations. In particular, by changing the light polarization from linear to right- or left-circular, the occurrence of spin-angular momentum transfer from light to the dust can be investigated (Donato et al. 2014; Jones et al. 2015). The forward-scattered light from a trapped particle, containing information about the particle position, is collected together with the transmitted light by a condenser. The superposition of these two beams generates an interferometric pattern, which is reflected by a second dichroic mirror toward a QPD through a lens (l_3) as shown in Figure 1(e) (Jones et al. 2015; Polimeno et al. 2018). A QPD converts the interferometric pattern collected by a condenser in analogical voltage signals, proportional to the displacement of the particle from its equilibrium position (Gittes & Schmidt 1998; Jones et al. 2015; Magazzù et al. 2015). The signals from the QPD were acquired at a sampling frequency of 50 kHz by a National Instrument acquisition board for time intervals of 2 s. The sampled signals were then analyzed by a PC providing information about the opto-mechanical interaction between light and a single grain of cosmic dust.

In order to characterize the optical trapping forces on a single dust grain, we extract some crucial parameters from the particle random trajectories in the confining potential, such as the trap relaxation frequency. The starting point of optical force measurements in OT is the description of the center-of-mass random motion of an optically trapped particle through an overdamped Langevin equation (Jones et al. 2015). In particular, for small displacements around the equilibrium point, a positional coordinate, e.g., x , of the trapped particle, subject to the random force, $F_{\text{random}}(t)$, can be expressed in terms of the

following equation:

$$\gamma \frac{dx}{dt} + \kappa_x x = F_{\text{random}}(t) \quad (\text{B1})$$

where γ is the Stokes friction coefficient of a particle immersed in a fluid medium, and κ_x is the trap stiffness that we wish to measure. The first term of Equation (B1) is the velocity-dependent viscous force, the second one is the restoring term due to the optical potential, and the final one describes the Brownian stochastic force. The PSD of a signal describes how its energy is distributed in the frequency domain, and it is useful to calibrate OT. Indeed, the PSD of Equation (B1) shows a Lorentzian shape:

$$S_x(\omega) = \frac{2D}{(\omega^2 + \omega_x^2)} \quad (\text{B2})$$

where the half-width of the distribution is the relaxation frequency defined as $\omega_x = \kappa_x/\gamma$, and $D = k_B T/\gamma$ is the diffusion coefficient from the Stokes–Einstein equation (Jones et al. 2015). By fitting the power spectrum of the particle coordinate with a Lorentzian shape function, see Figure 6(b), we obtain the relaxation frequency ω_x as a fit parameter, and hence we can get the trap spring constant, κ_x (Gittes & Schmidt 1998; Magazzù et al. 2015).

The Raman tweezers used for the identification of the minerals constituting our samples is a customized setup obtained by coupling a homemade OT with a commercial Raman spectrometer (Horiba TRIAX 190) through a notch filter; see Figure 1(f). This filter reflects the laser light, from an LD having a wavelength of 785 nm, to the back aperture of an oil immersion objective, similarly to the case of the dichroic mirror previously described in the standard OT setup; see Figure 1(e). The notch filter reflects only the single wavelength of the laser beam, and it is transparent to all the other wavelengths. In such a way, the elastic component of the scattering is cut out by the notch filter, and only the Raman signal is transmitted to the spectrometer, which is equipped with a grating having a spectral resolution of 8 cm^{-1} and coupled to a silicon Peltier-cooled CCD camera to acquire the spectra. The Raman spectra of our investigated samples were obtained with a laser power of about 7 mW at the sample and acquired with an integration time of a few tens of seconds.

Appendix C Theoretical Calculations

C.1. Radiation Force in Optical Tweezers

In the framework of electromagnetic scattering theory, optical forces and optical trapping are the consequence of the electromagnetic momentum conservation during a light scattering process (Borghese et al. 2007a; Jones et al. 2015). Using the linear momentum conservation, the time-averaged optical force on a generic particle exerted by a monochromatic light is as follows:

$$\mathbf{F}_{\text{rad}} = \oint_S \bar{\mathbf{T}}_M \cdot \hat{n} dS \quad (\text{C1})$$

where the integration is carried out over a surface S surrounding the scattering particle, \hat{n} is the outward normal unit vector, and $\bar{\mathbf{T}}_M$ is the averaged Maxwell stress tensor in the Minkowski form (Pfeifer et al. 2007) describing the opto–mechanical interaction. For a nonmagnetic medium (Borghese et al. 2007a),

$$\mathbf{F}_{\text{rad}} = -\frac{\varepsilon_m r^2}{4} \int_{\Omega} \left(|\mathbf{E}_s|^2 + \frac{c^2}{n_m^2} |\mathbf{B}_s|^2 + 2\Re \left\{ \mathbf{E}_i \cdot \mathbf{E}_s^* + \frac{c^2}{n_m^2} \mathbf{B}_i \cdot \mathbf{B}_s^* \right\} \right) \hat{r} d\Omega \quad (\text{C2})$$

where $\varepsilon_m = \varepsilon_0 n_m^2$ is the medium permittivity, r and \hat{r} are the modulus and the unit vector of the vector position \vec{r} respectively, ε_0 is the vacuum permittivity, n_m is the medium refraction index, c is the light velocity, and \mathbf{E}_i , \mathbf{B}_i , \mathbf{E}_s , \mathbf{B}_s are respectively the incident electric and magnetic field and the scattered electric and magnetic field, and the integration is taken over the full solid angle Ω . The scattered electromagnetic field \mathbf{B}_s is calculated in near zone, taking into account the transmission properties of the wave inside the nanoparticle. When we deal with spherical monomers, the expression of the radiation force should be rewritten in terms of T-matrix formalism (Saija et al. 2005; Borghese et al. 2007a; Polimeno et al. 2018). Because of the linearity of Maxwell’s equations, once the field involved in the scattering process is expanded in terms of vector Helmholtz harmonics (VHH), it is possible, through the definition of T-matrix, to obtain the relation between the incident and scattered field imposing the boundary conditions to the fields on the spherical surface (Borghese et al. 2007b). The T-matrix $\mathbb{T} \equiv \{T_{l'm'l}^{(p,p)}\}$ elements encompass all the information on the morphology of the scattering particle with respect to the incident field, binding the known multipole amplitudes of the incident field $W_{i,lm}^{(p)}$ with the unknown amplitudes of the scattered field $A_{s,l'm'}^{(p)}$ (Borghese et al. 2007a). For the case of OT, we generalized the incident field resorting to the angular spectrum representation of Richards and Wolf (Richards & Wolf 1959) and then calculated the OT stiffness for each particle (Borghese et al. 2007b; Jones et al. 2015).

C.2. Optical Properties of Composite Particles

Knowledge of the optical properties of particles that interact with radiation is a key ingredient for the correct modeling of a matter–radiation interaction. When the medium that constitutes the particles is a multicomponent mixture, two main paths can be taken for modeling: (1) homogenization theory (Garnett 1904, 1906) through the use of the Bruggeman mixing formula

(Bruggeman 1935, 1936); (2) the representation of complexity by means of a random geometry of one-component inclusions whose size can respect the fraction of volume obtained from the experimental chemical–physical analysis of the sample. The Bruggeman mixing formula (Bruggeman 1935, 1936) can be applied to a medium composed of N kinds of inclusions with permittivities ε_n and volume fractions f_n such that $\sum_n f_n = 1$. In this case, unlike the Maxwell–Garnett mixing formula that is inapplicable when the volume fractions of all components are comparable, the Bruggeman mixing formula is symmetric with respect to all medium components and does not treat any one of them differently. Therefore, it can be applied, at least formally, to composites with arbitrary volume fractions without causing contradictions when we cannot distinguish the *host* material from the *inclusions*. From an operative point of view, the Bruggeman effective permittivity, which we denote by ε_{BG} , can be obtained by satisfying the following equation:

$$\sum_{n=1}^N f_n \frac{\varepsilon_n - \varepsilon_{BG}}{\varepsilon_n + 2\varepsilon_{BG}} = 0 \quad (\text{C3})$$

where $\sum_n f_n = 1$. In the case of a strongly inhomogeneous particle consisting of islands of different materials, the process of interaction underlying the optical trapping phenomena is reminiscent of the multicomponent structure of the nanoparticle, and the formula of Bruggeman, derived within the homogenization theory, tends to mask this behavior. For this purpose, the optical behaviors of the spherical inclusions contained within the spherical nanoparticle, which constitute an aggregate, are studied by applying the theory of electromagnetic scattering to clusters of spheres.

Within the T-matrix approach, the computation of the multipole amplitudes of the field scattered by the whole object is performed in two steps. First, we consider the superposition of the field that would exist within the sphere in absence of any inclusion and of the scattered fields coming from the aggregate taking into account all the multipolar interactions. This superposition constitutes the internal field of the host sphere. Second, we impose the boundary conditions to the internal field and to the external field across the surface of the host sphere to get the amplitudes of the scattered field.

As a result of the first step, we get a system of linear non-homogeneous equations that in symbolic form can be written as follows:

$$\mathbb{P} = \mathbb{Z}\mathbb{W} \quad (\text{C4})$$

where \mathbb{P} is the matrix whose elements are the unknown scattering coefficients of the internal field to be calculated, \mathbb{Z} is the T-matrix of the internal aggregate, and \mathbb{W} is the matrix of the known, external incident field coefficients.

Once the amplitudes of \mathbb{P} have been calculated, we proceed to the second step, which in symbolic form yields:

$$\mathbb{A} = \mathbb{S}\mathbb{P} = \mathbb{S}(\mathbb{Z}\mathbb{W}) = \mathbb{T}\mathbb{W} \quad (\text{C5})$$

where \mathbb{A} is the matrix whose elements are the scattering coefficients in the external medium to be calculated, \mathbb{S} is the matrix that acts on the matrix \mathbb{P} containing the coefficients of the already-calculated internal field, and \mathbb{T} is the transition matrix for the whole scatterer (Borghese et al. 1994, 1998).

Appendix D Samples Characterization

The samples used in this work (M-26, HE-1, A-1, DEW 12007) have been analyzed under the field emission scanning electron microscope with energy dispersive spectroscopy FEG-SEM FEI QUANTA 450 at CISUP for a textural characterization (shape, grain-size). Their main mineralogic composition is determined using X-ray powder diffraction data acquired at the Dipartimento di Scienze della Terra of the Università di Pisa. The lithology and mineralogic composition of the samples are reported in Table 1.

The characterization of M-26 refers to Fazio et al. (2014). In-depth characterization of DEW 12007 can be found in Collareta et al. (2016). Quantitative mineralogical compositions of the

samples M-26 (quartzarenite), HE-1 (hawaiite), A-1 (carbonaceous chondrite Allende), and DEW 12007 (lunar regolith breccia) were obtained applying the Rietveld method (Bish & Post 1993) and given in Table 1. X-ray powder diffraction data were collected at the Dipartimento di Scienze della Terra of the Università di Pisa, on a Bruker D2 phaser diffractometer, equipped with a Lynxeye detector, operating at 30 kV and 10 mA and using Cu K α radiation ($\lambda=1.54184$ Å). The diffraction patterns were collected over the 5°–70° 2θ range for DEW 12007 and 12°–70° 2θ range for HE-1 and Allende, with 0.02° scan step size and 1 s counting time per step. Samples were spiked with a known amount of rutile as an internal Standard Reference Material (NIST SRM 674a) in order to check for the presence of an amorphous component (Gualtieri 2000).








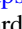






Table 1

Textural and Mineralogic Composition of the Samples Used to Test the Raman Tweezers Set-up: (1) M-26, Quartzarenite; (2) HE-1 Hawaiite; (3) A-1 Allende; (4) DEW 12007

| Sample | Lithology | Overall Min. Compo. Weight (%) |
|--------------------|---|---|
| M-26 | Quartzarenite—coarse-grained | Quartz > 99 |
| HE-1 | Hawaiite—fine-grained; basalt with pyroxene and plagioclase microphenocrysts with abundant glass; vesicular; 30% phenocrysts by volume | Plagioclase: labradorite, 56 Clinopyroxene: augite, 35 Olivine: forsterite, 8; magnetite < 1; glass < 5 |
| Allende (A-1) | CV3 OxA carbonaceous chondrite—chondrules and calcium-aluminum-rich inclusions (~55% by volume) embedded in a fine-grained dark matrix (~40% by volume) | Olivine: forsterite, 80 Clinopyroxene: clinoenstatite, 9 Clinopyroxene: diopside, 7 Orthopyroxene: enstatite, 2 Clinopyroxene: pigeonite, 1; chromite < 1 |
| DeWitt (DEW) 12007 | Lunar polymictic breccia with <1 mm sized lithic clasts in fine grained fragmental matrix | Plagioclase: labradorite, 48 Clinopyroxene: augite, 23 Clinopyroxene: pigeonite, 18 Olivine: forsterite, 10; Ilmenite, 1; chromite, < 1 |

Note. For each sample, the following is reported: (1) its lithology (type of rock and textural information) obtained at the FEG-SEM and literature and (2) the overall mineralogical composition [weight percent] obtained with X-ray diffraction.

ORCID iDs

A. Magazzù  <https://orcid.org/0000-0003-1247-2702>
 D. Bronte Ciriza  <https://orcid.org/0000-0002-5874-6601>
 A. Musolino  <https://orcid.org/0000-0003-1238-0445>
 A. Saidi  <https://orcid.org/0000-0002-1999-3239>
 P. Polimeno  <https://orcid.org/0000-0003-3847-5274>
 M. G. Donato  <https://orcid.org/0000-0002-7580-3137>
 A. Foti  <https://orcid.org/0000-0002-9824-3099>
 P. G. Gucciardi  <https://orcid.org/0000-0003-1826-9174>
 M. A. Iatì  <https://orcid.org/0000-0002-3576-8656>
 R. Saija  <https://orcid.org/0000-0002-5823-9749>
 N. Perchiazzi  <https://orcid.org/0000-0003-3229-2282>
 A. Rotundi  <https://orcid.org/0000-0001-5467-157X>
 L. Folco  <https://orcid.org/0000-0002-7276-3483>
 O. M. Maragò  <https://orcid.org/0000-0002-7220-8527>

References

- Alali, H., Gong, Z., Videen, G., et al. 2020, *JQSRT*, **255**, 107249
 Ashkin, A., & Dziedzic, J. M. 1971, *ApPhL*, **19**, 283
 Ashkin, A., Dziedzic, J. M., Bjorkholm, J. E., & Chu, S. 1986, *OptL*, **11**, 288
 Bish, D. L., & Post, J. E. 1993, *AmMin*, **78**, 932
 Bohren, C. F., & Huffman, D. R. 2008, Absorption and scattering of light by small particles (New York, NY: Wiley)
 Borghese, F., Denti, P., & Saija, R. 1994, *ApOpt*, **33**, 484
 Borghese, F., Denti, P., & Saija, R. 2007a, Scattering from model nonspherical particles: theory and applications to environmental physics (Berlin: Springer), doi:10.1007/978-3-540-37414-5
 Borghese, F., Denti, P., Saija, R., & Iatì, M. A. 2007b, *OExpr*, **15**, 11984
 Borghese, F., Denti, P., Saija, R., Iatì, M. A., & Sindoni, O. I. 1998, *JOpt*, **29**, 28
 Brownlee, D., Tsou, P., Anderson, J., et al. 2003, *JGRE*, **108**, 8111
 Brunetto, R., Lantz, C., Ledu, D., et al. 2014, *Icar*, **237**, 278
 Bruggeman, D. A. G. 1935, *AnP*, **416**, 636
 Bruggeman, D. A. G. 1936, *AnP*, **417**, 645
 Calura, F., Pipino, A., & Matteucci, F. 2008, *A&A*, **479**, 669
 Colangeli, L., Lopez-Moreno, J. J., Palumbo, P., et al. 2007, *SSRv*, **128**, 803
 Collareta, A., D’Orazio, M., Gemelli, M., Pack, A., & Folco, L. 2016, *M&PS*, **51**, 351
 Cristofolini, R., Menzies, M. A., Beccaluva, L., & Tindle, A. 1987, *BVol*, **49**, 599
 Davidson, J., Busemann, H., & Franchi, I. A. 2012, *M&PS*, **47**, 1748
 Della Corte, V., Palumbo, P., Rotundi, A., et al. 2012, *SSRv*, **169**, 159
 Della Corte, V., Rietmeijer, F. J. M., Rotundi, A., & Ferrari, M. 2014, *AsBio*, **14**, 694
 Donato, M. G., Hernandez, J., Mazzulla, A., et al. 2014, *NatCo*, **5**, 3656
 Draine, B. T. 2003, *ARA&A*, **41**, 241
 Fazio, A., Folco, L., D’Orazio, M., Frezzotti, M. L., & Cordier, C. 2014, *M&PS*, **49**, 2175
 Floss, C., Stadermann, F. J., Bradley, J. P., et al. 2006, *GeCoA*, **70**, 2371
 Folco, L., & Cordier, C. 2015, Planetary Mineralogy (London: European Mineralogical Union), doi:10.1180/EMU-notes 15.9
 Frank, D. R., Westphal, A. J., Zolensky, M. E., et al. 2014, *M&PS*, **49**, 1522
 Garnett, J. C. M. 1906, *RSPTA*, **205**, 237
 Garnett, J. C. M. 1904, *RSPTA*, **203**, 385
 Genge, M. J., Engrand, C., Gounelle, M., & Taylor, S. 2008, *M&PS*, **43**, 497
 Gieseler, J., Gomez-Solano, J. R., Magazzù, A., et al. 2021, *AdOP*, **13**, 74
 Gillibert, R., Balakrishnan, G., Deshoules, Q., et al. 2019, *EnST*, **53**, 9003
 Gittes, F., & Schmidt, C. F. 1998, *OptL*, **23**, 7
 Gong, Z., Pan, Y.-L., Videen, G., & Wang, C. 2018, *JQSRT*, **214**, 94
 Irrera, A., Magazzù, A., Artoni, P., et al. 2016, *NanoL*, **16**, 4181
 Jones, P. H., Marago, O. M., & Volpe, G. 2015, Optical tweezers: Principles and applications (Cambridge: Cambridge Univ. Press)
 Jones, P. H., Palmisano, F., Bonaccorso, F., et al. 2009, *ACS Nano*, **3**, 3077
 Lankers, M., Popp, J., & Kiefer, W. 1994, *ApSpe*, **48**, 1166
 Lauretta, D. S., Balram-Knutson, S. S., Beshore, E., et al. 2017, *SSRv*, **212**, 925
 Lewis, R. S., Ming, T., Wacker, J. F., Anders, E., & Steel, E. 1987, *Natur*, **326**, 160
 Lodders, K., & Amari, S. 2005, *Geoch*, **65**, 93
 Mackinnon, I. D. R., & Rietmeijer, F. J. M. 1987, *RvGeo*, **25**, 1527
 Magazzù, A., Spadaro, D., Donato, M. G., et al. 2015, *Rendiconti Lincei*, **26**, 203
 Marston, P. L., & Crichton, J. H. 1984, *PhRvA*, **30**, 2508
 Orlando, A., D’Orazio, M., Armienti, P., & Borriani, D. 2008, *EJMin*, **20**, 653
 Pan, Y.-L., Hill, S. C., & Coleman, M. 2012, *OExpr*, **20**, 5325
 Pesce, G., Volpe, G., Luca, A. C. D., Rusciano, G., & Volpe, G. 2009, *EL*, **86**, 38002
 Pfeifer, R. N. C., Nieminen, T. A., Heckenberg, N. R., & Rubinsztein-Dunlop, H. 2007, *RvMP*, **79**, 1197
 Polimeno, P., Magazzù, A., Iatì, M., et al. 2021, *EPJP*, **136**, 339
 Polimeno, P., Magazzù, A., Iatì, M. A., et al. 2018, *JQSRT*, **218**, 131
 Rauf, K., Hann, A., Wallis, M., & Wickramasinghe, C. 2010, *IJA&B*, **9**, 183
 Richards, B., & Wolf, E. 1959, *RSPSA*, **253**, 358
 Rietmeijer, F. J. 1998, Planetary Materials, Vol. 36 (Berlin: De Gruyter), 2 29
 Rietmeijer, F. J. M. 2001, *P&SS*, **49**, 71
 Rotundi, A., Baratta, G., Borg, J., et al. 2008, *M&PS*, **43**, 367
 Saija, R., Antonia Iatì, M., Giusto, A., Denti, P., & Borghese, F. 2005, *JQSRT*, **94**, 163
 Schmidt, F., Magazzù, A., Callegari, A., et al. 2018, *PhRvL*, **120**, 068004
 Smith, C. L., Russell, S. S., Hutzler, A., et al. 2021, Sample Return Missions (Amsterdam: Elsevier), 249
 Swartzlander, G. A., Peterson, T. J., Artusio-Glimpse, A. B., & Raisanen, A. D. 2011, *NaPho*, **5**, 48
 Taylor, A. D., Baggaley, W. J., & Steel, D. I. 1996, *Natur*, **380**, 323
 Taylor, S., Messenger, S., & Folco, L. 2016, *Elem*, **12**, 171
 Testa, J. P., Stephens, J. R., Berg, W. W., et al. 1990, *E&PSL*, **98**, 287
 Thurn, R., & Kiefer, W. 1984, *ApSpe*, **38**, 78
 Westphal, A. J., Stroud, R. M., Bechtel, H. A., et al. 2014, *Sci*, **345**, 786
 Woosley, S. E., Heger, A., & Weaver, T. A. 2002, *RvMP*, **74**, 1015
 Woosley, S. E., & Weaver, T. A. 1995, The evolution and explosion of massive Stars II: Explosive hydrodynamics and nucleosynthesis, Lawrence Livermore National Lab., CA (United States), doi:10.2172/115557